Title:

S1P regulates intervertebral disc aging by mediating endoplasmic reticulum - mitochondrial calcium ion homeostasis

Bingjie Zheng[1,2,3#], Xuyang Zhang[1,2,#], Xiangxi Kong[1,2,#], Jie Li[4], Bao Huang[1,2], Hui Li[1,2], Zhongyin Ji[1,2], Xiaoan Wei[1,2], Siyue Tao[1,2], Zhi Shan[1,2], Zemin Ling[5], Junhui Liu[1,2,*], Jian Chen[1,2,6*], Fengdong Zhao[1,2,6*]

1. Department of Orthopaedic Surgery, Sir Run Run Shaw Hospital, Zhejiang University School of Medicine, Hangzhou, Zhejiang, 310027, China.
2. Key Laboratory of Musculoskeletal System Degeneration and Regeneration Translational Research of Zhejiang Province, Hangzhou, Zhejiang, 310027, China.
3. The First Affiliated Hospital of USTC, Division of Life Sciences and Medicine, University of Science and Technology of China, Hefei, Anhui, 230001, China.
4. Department of Orthopaedic Surgery, Ningbo Medical Center Li Huili Hospital, Ningbo, China.
5. Shenzhen Key Laboratory of Bone Tissue Repair and Translational Research, Department of Orthopaedic Surgery, The Seventh Affiliated Hospital of Sun Yat-sen University, Shenzhen, 518107, China.
6. Department of Wound Healing, The First Affiliated Hospital of Wenzhou Medical University.

# These authors contributed equally to this work.

Corresponding authors: Fengdong Zhao, E-mail: zhaofengdong@zju.edu.cn; Jian Chen, E-mail: chenjian-bio@zju.edu.cn; Junhui Liu, E-mail: ljhzju@zju.edu.cn.

Abstract:

As the aging process progresses, age-related intervertebral disc degeneration (IVDD) is becoming an emerging public health issue. Site-1 protease (S1P) has recently been found to be associated with abnormal spinal development in mutant patients and has multiple biological functions. Here, we discovered a reduction of S1P in degenerated and aging intervertebral discs, primarily regulated by DNA methylation. Furthermore, through drug treatment and siRNA mediated S1P knockdown, nucleus pulposus cells were more prone to exhibit degenerative and aging phenotypes. Conditional knockout of S1P in mice resulted in spinal developmental abnormalities and premature aging.

Mechanistically, S1P deficiency impeded COP II-mediated transport vesicles formation, which leads to proteins retention in the endoplasmic reticulum (ER) and subsequently ER distension. ER distension increased the contact between the ER and mitochondria, disrupting ER-to-mitochondria calcium flow, resulting in mitochondrial dysfunction and energy metabolism disturbance. Finally, using 2-APB to inhibit calcium ion channels and the senolytic drug dasatinib and quercetin (D + Q) partially rescued the aging and degenerative phenotypes caused by S1P deficiency. In conclusion, our findings suggest that S1P is a critical factor in causing IVDD in the process of aging and highlight the potential of targeting S1P as a therapeutic approach for age-related IVDD.

Keywords: Intervertebral disc, aging, Site-1 protease

Introduction

As the aging population continues to grow, aging-related diseases are becoming a global epidemic (1). Among the health challenges, age-related intervertebral disc degeneration (IVDD) (2) stands out as one of the most significant chronic conditions. Aging intervertebral disc (IVD) is characterized by a significant reduction in the microvascular network of the cartilaginous endplate (CEP), leading to decreased thickness and altered permeability. Within this context, nucleus pulposus (NP) exhibit an aging-related secretory phenotype, with reduced anabolism and increased catabolism. These aging NP cells also secrete various inflammatory factors, further exacerbating the process of IVDD (3–5). Age-related IVDD can lead to the development of low back pain, affecting individuals' quality of life, imposing a substantial economic burden on society (6). Therefore, gaining a comprehensive understanding of the biological mechanisms underlying IVD aging and developing therapeutic approaches holds crucial clinical significance in addressing age-related IVDD.

Site-1 protease (S1P) is a serine protease belonging to the proprotein convertase subtilisin / kexin family, also known as kexin-like protease-1 (SKI-1) (7, 8). Encoded by the membrane-bound transcription factor peptidase site 1 (MBTPS1) gene, it primarily localizes to the Golgi apparatus (9) and plays a crucial role in autophagy (10), lipid metabolism and endoplasmic reticulum homeostasis (11, 12). Mice lacking S1P globally experience embryonic lethality prior to implantation (12). Moreover, S1P is essential for ECM signaling, axial elongation, and vertebral development during mitosis (13). Research has indicated that patients with mutations in the S1P gene exhibit

skeletal developmental abnormalities and spinal deformities such as scoliosis (14). However, the impact of S1P on IVDs has not been investigated.

Cell senescence involves the gradual deterioration of tissue structure and function, encompassing cell apoptosis, decreased cell function, and inflammation within the tissue. Calcium homeostasis and mitochondrial oxidative damage are critical factors contributing to tissue degeneration (15). Aberrations in intracellular calcium ion homeostasis can lead to disruptions in cell signaling, energy metabolism, and antioxidant defense mechanisms, ultimately compromising cellular function and potentially triggering cell aging (16, 17). Oxidative damage can result in a decrease in mitochondrial membrane potential, impairments in the electron transport chain, and an increased generation of reactive oxygen species. These factors contribute to mitochondrial dysfunction, further accelerating the aging processes at the cellular and tissue levels (18, 19).

In this study, we investigated the role of S1P in the process of IVD aging and degeneration. Our findings revealed that S1P is downregulated in the process of IVD aging and degeneration due to increased DNA methylation level. The absence of S1P affects process of cellular proteins transport, leading to abnormal endoplasmic reticulum (ER) swelling, subsequently resulting in increased ER-mitochondria contacts and calcium flux. This in turn leads to mitochondrial oxidative stress and functional damage, ultimately contributing to IVD aging and degeneration. These findings suggest that S1P could be a potential target for improving and treating age-related IVDD.

Results

The expression of S1P decreases in degenerated and aged IVD.

We collected clinical samples of human degenerated IVD tissues and observed that within the normal subgroup, there was a higher expression of S1P. However, as the degree of degeneration increased (Figure 1A), the proportion of S1P immunopositive cells gradually decreased. We isolated NP cells from collected clinical samples of human degenerated IVDs and extracted RNA. The mRNA expression levels of S1P demonstrates a significant decrease in Pfirrmann Grades III, IV, and V degeneration groups when compared to the Pfirrmann Grade II degeneration group (Figure 1B).

To further validate the expression of S1P in degenerated IVDs, we established a mice tail needle-punctured degeneration model. As illustrated in (Figure 1C), in comparison to the sham group, mice subjected to the degeneration induction for 4 weeks exhibited a pronounced IVD degeneration phenotype, meanwhile there was a significant reduction proportional reduction in the number of S1P immunopositive cells (Figure 1D). Subsequently, we induced degeneration in primary NP cells in vitro to assess the expression levels of S1P. The protein expression of S1P exhibited a significant decrease following IL-1β induction compared to the NC group (Figure 1E). The qPCR results confirmed the trend observed in the protein blot (Figure 1F).

Additionally, we observed a decrease in the expression level of S1P in aging IVD tissues. Immunofluorescence analysis of young mice aged 6 weeks displayed widespread expression of S1P, whereas immunofluorescence analysis of naturally old mice at 24 months revealed a greater number of NP cells lacking immunopositivity for S1P (Figure

1, G and H). We observed cell senescence progressively increases with passage number and there was a concomitant decrease in S1P expression (Supplemental Figure 1A). Moreover, we performed an in vitro validation of NP cell aging by inducing it with H_2O_2. Based on the results of the CCK8 assay (Supplemental Figure 1B), treatment with 200 μM H_2O_2 led to a significant decrease in cell proliferation activity, whereas treatment with 100 μM H_2O_2 preserved cell proliferation activity to a greater extent. Thus, we chose a concentration of 100 μm H_2O_2 to induce NP cell aging. We mapped the expression patterns of senescence-associated secretory phenotype (SASP) that exhibited differential expression after treating with 100 μm H_2O_2 for different hours followed by 5 days of continued culture to induce aging, and observed the expression of S1P significantly decreased both at the protein expression level (Figure 1I) and the mRNA level (Supplemental Figure 1, C-G). Together, S1P expression decreased in degenerated and aging IVD, both at the tissue and cellular levels, suggesting a potential link between S1P and disc degeneration.

DNA methylation regulates the gene expression of S1P in aging NP cells.

Based on literature research, it has been found that the process of cellular aging is accompanied by diverse changes in DNA methylation. In certain tissues, specific genes exhibit high levels of methylation during aging, leading to a gradual reduction in their transcriptional levels and eventual gene silencing (20). Therefore, we hypothesize that gene expression of S1P was regulated through methylation mechanisms in aging NP cells. We observed that after inducing aging in NP cells through H_2O_2 treatment, there were varying degrees of increased expression of the methylation transferases DNMT3a

(Figure 2A). Subsequently, utilizing Methylation-Specific PCR (MSP) experiments, we found a significant increase in the gene methylation levels of S1P under H_2O_2 induction (Figure 2B). The brightness of the agarose gel band representing methylated S1P DNA (M) increased noticeably compared to the NC group, while the brightness of the agarose gel band representing unmethylated S1P DNA (U) weakened. Treatment with the methylation inhibitor 5-AZA led to a reduction in the brightness of the agarose gel band representing methylated S1P DNA (M). Furthermore, we performed Bisulfite Sequencing PCR following sodium bisulfite treatment (BSP) experiments to validate the methylation sites within S1P promoter region in aging NP cells. As illustrated in (Figure 2C), based on computational predictions, there are 14 potential CpG islands within the S1P promoter region. In the NC group, only 4.3% of CpG islands in the S1P promoter were methylated, while after H_2O_2 treatment, 37.9% of CpG islands exhibited methylation. This provides evidence that the promoter region of S1P in aging NP cells experiences high levels of methylation, consequently leading to reduced expression of the S1P. Treatment with 5-AZA resulted in a reduction in the methylation percentage of CpG islands.

After confirming the high methylation of the S1P promoter region in aging NP cells, we treated H_2O_2-induced aging NP cells with different concentrations of the methylation inhibitor 5-AZA. We found that it significantly rescued the downregulation of S1P in aging NP cells (Figure 2D). Additionally, we observed that after rescuing the downregulation of S1P through 5-AZA treatment, there was a partial rescue of the degenerative phenotype in NP cells (Figure 2E).

To further elucidate which methylation transferases are responsible for the downregulation of S1P expression in aging NP cells, we employed siRNA to knock down different methylation transferases. We found that knocking down of the methylation transferase DNMT3a significantly rescued the decrease in S1P levels after H_2O_2-induced aging (Figure 2F). Thus, in aging NP cells, the primary mechanism underlying the reduction of S1P is mediated by DNMT3a, which promotes DNA methylation of the S1P gene.

The absence of S1P leads to IVD degeneration and premature aging.

Since the expression of S1P is downregulated in both degenerated and aging NP cells, further exploration is necessary to uncover the role of S1P in IVDs. We employed the specific inhibitor PF 429242 to suppress S1P function and found that it led to a decrease in anabolism markers (Col2 and SOX9) and an increase in catabolism markers (ADAMTS5 and MMP13) in NP cells (Figure 3, A and B). Meanwhile, we observed that the severity of the degenerative phenotype increased with higher concentrations of PF 429242 usage (Supplemental Figure 2, A-F). Although the PF 429242 inhibitor exhibits high selectivity for S1P, it could potentially affect unknown targets. Hence, we further validated the impact of S1P on NP cells by specifically knocking down S1P using S1P siRNA. Upon S1P knockdown, similar to the trend observed with the PF 429242 inhibitor, NP cells exhibited a clear degenerative phenotype (Figure 3, C and D). Meanwhile, the knockdown of S1P resulted in decreased Alcian blue staining in NP cells (Figure 3E). Moreover, we performed a rescue experiment by transfecting an S1P overexpression plasmid. This rescue approach successfully restored the deficiency of

S1P and was found to rescue the anabolic and catabolic processes in NP cells (Figure 3F). This rescue strategy improved the decreased Alcian blue staining observed in NP cells (Figure 3G).

Furthermore, During the process of cellular senescence, cells undergo DNA damage, decreased cell proliferation, and increased SA-β-gal activity. We examined these early markers of cellular senescence. We observed that after S1P knockdown, the proportion of SA-β-Gal-positive cells in NP cells increased over time (Figure 3, H and I). We analyzed the expression of aging-related markers in NP cells six days after siRNA knockdown of S1P and verified a significant increase in the expression of these markers compared to the NC group (Figure 3J).

We discovered that after knocking down S1P, NP cells are more prone to exhibit an aging phenotype under the same conditions of H_2O_2 induction. Using EdU to detect cell proliferation levels, we observed a significant decrease in the proportion of EdU-positive NP cells after both S1P knockdown and H_2O_2 treatment. However, among NP cells subjected to H_2O_2 treatment after S1P knockdown, the proportion of EdU-positive cells exhibited a more pronounced decrease compared to either the S1P knockdown group or the H_2O_2 treatment group (Figure 3, K and L). This indicated that both individual S1P knockdown and individual H_2O_2 treatment impact the proliferation rate of NP cells, while S1P knockdown enhanced the effect of H_2O_2 on the proliferation activity of NP cells. Through flow cytometry analysis, we observed a significant increase in the proportion of cells in the S/G2 phase in the H_2O_2-induced group with S1P knockdown compared to the other groups, indicating cell cycle arrest (Figure 3, M

and N). To further assess the cellular aging phenotype, we performed γ-H2A.X fluorescence staining to examine the DNA damage status. Compared to the NC group, NP cells with S1P knockdown exhibited a significant increase in γ-H2A.X fluorescence intensity under the same H_2O_2 treatment conditions (Figure 3O). In summary, the above experiments indicate that knocking down S1P sensitizes NP cells to the aging-inducing effects of H_2O_2, leading to more pronounced manifestation of cellular aging phenotypes at earlier stage. This suggested that S1P played a crucial role in regulating the response of NP cells to aging-related stressors.

S1P conditional knockout mice exhibit a more severe degenerative phenotype and experience premature aging.

To investigate the impact of S1P on IVD during growth and development, we established Shh-Cre-$S1P^{f/f}$ mice. Unexpectedly, we found that homozygous Shh-Cre-$S1P^{f/f}$ mice exhibited embryonic lethality. Alizarin red/Alcian blue-stained embryos demonstrated that the body segments of these homozygous Shh-Cre cKO mice displayed a significantly reduced development length (Figure 4A). Furthermore, Alcian Blue staining of the IVD region exhibited a noticeably lighter coloration in these homozygous Shh-Cre cKO mice, indicating abnormal cartilage development (Figure 4B). Despite our discovery that Shh-Cre-$S1P^{f/f}$ homozygous knockout mice exhibit embryonic lethality, we did not observe significant pathological abnormalities in vital organs such as the heart and lungs of the heterozygous mice (Supplemental Figure 3A). Additionally, we used S1P immunofluorescence images to demonstrate the knockout efficiency in NP tissue (Supplemental Figure 3B). Therefore, we speculated that the

cause of embryonic lethality might be due to restricted somite development, which could affect the organogenesis of fetal mice.

Subsequently, when we cultured heterozygous S1P knockout mice with Shh-Cre, they exhibited noticeable dwarfism. At the age of 2 weeks, their body length was significantly shorter compared to the littermate control mice (Figure 4C). The DHI% revealed that IVDD was notably restricted (Figure 4D). Meanwhile, through histological staining, we found a significant reduction in the nucleus pulposus area of the IVDs in the heterozygous knockout mice (Figure 4E). Furthermore, there was a notable decrease in the mean fluorescence intensity of Col2, indicative of decreased anabolism and a significant increase of the mean fluorescence intensity of MMP13, indicative of catabolism (Figure 4, E and F).

To further investigate the influence of S1P on IVD degeneration and aging, we conditional knocked out S1P by generating Acan-CreERT-S1P$^{f/f}$ mice through the injection of tamoxifen for five consecutive days in 8-week-old mice. Meanwhile, we used S1P immunofluorescence images to demonstrate the knockout efficiency in NP tissue (Supplemental Figure 3C). Subsequently, an IVD degeneration model by tail-looping was established at age of 12 weeks. Compared to the littermates control group, the degenerative phenotype was more pronounced in the Acan-CreERT-S1P$^{f/f}$ mice, with a significant difference in histological scores (Figure 4, G and H). This indicates that specific knockout of S1P in IVD could accelerate the process of IVDD. Furthermore, we observed a significant increase in p16-immunopositive regions in Acan-Cre cKO mice after 15 months of normal feeding (Figure 4, I and J). Additionally,

these Acan-Cre cKO mice exhibited a more pronounced SASP, including a significant decrease in Col2-immunopositive regions and a significant increase in MMP13-immunopositive regions (Figure 4, I and K). In conclusion, the results above indicated that the knockout of S1P significantly affected the growth and development of IVDs and led to a more severe IVDD phenotype and an earlier manifestation of aging-related characteristics.

The absence of S1P disrupts intracellular proteins transport homeostasis in NP cells and leads to an increase in endoplasmic reticulum-mitochondria contacts.

It has been known that S1P plays a significant role in ER stress and unfolded protein response. We mapped the expression patterns of representative genes from three pathways related to ER stress and unfolded protein response. We observed a reduction in the mature form of ATF6α (m-ATF6α) in the ATF6α pathway after knocking down S1P. The expression of XBP-1 in the IRE1α pathway also decreased. There was no significant change in ATF4, a component of the PERK pathway as well as BIP, a molecular chaperone protein involved in the unfolded protein response (21). Furthermore, the expression of CHOP, a marker for late-stage ER stress-induced apoptosis, remained unchanged (Figure 5A). We confirmed this expression trend after treatment with different concentrations of the PF 429242 as well (Supplemental Figure 4A). CHOP has been confirmed as a signal for ER stress-induced apoptosis, inducing apoptosis under severe ER stress (22). This suggested that the absence of S1P primarily triggers early changes in ER stress, without reaching the level of severe stress that guides apoptosis. Therefore, the absence of S1P did not seem to induce IVD aging

through ER stress. According to literature research, ATF6α and XBP-1 are involved in vesicular transport and COP II-related genes (23–25). Therefore, after inhibiting S1P with the inhibitor, we performed qPCR to assess the expression of COPII-related genes. We observed a downregulation in the gene expression of Sar1a and Sec23a (Figure 5B). The results from protein immunoblotting were consistent with the qPCR trends, showing a decrease in the expression of Sar1a and Sec23a upon S1P inhibition (Figure 5C). Also, we isolated human nucleus pulposus cells and conducted siRNA-mediated knockdown of S1P, followed by transcriptome analysis using next-generation sequencing (NGS) and identified negative regulation of COP II-related pathways through gene set enrichment analysis (Supplemental Figure 4B). These results suggested that the vesicular transport process in NP cells is affected upon S1P inhibition. Subsequently, we conducted immunofluorescence double staining of ER marker protein (Calnexin) and collagen protein (Col2) to assess the transport of large molecular proteins in NP cells with S1P knockdown. As shown in Figure 5D, upon S1P knockdown, the increased yellow co-localization regions compared to the NC group indicated substantial retention of Col2 protein within the ER. Additionally, protein retention within the ER led to changes in cellular morphology, with cells appearing visibly swollen compared to the NC group. Conversely, upon S1P overexpression, the reduced yellow co-localization regions compared to the S1P knockdown group suggested a rescuing effect associated with S1P overexpression. Furthermore, we conducted electron microscopy to examine the ER status in NP cells after S1P knockdown and found that the ER in NP cells following S1P knockdown exhibited

noticeable enlargement compared to the NC group (Figure 5E). This further supported the notion that the deficiency of S1P contributed to vesicular transport impairment, leading to protein retention within the ER and aberrant swelling of ER.

At the same time, we observed that upon knocking down S1P, the length of mitochondria-ER membrane contacts (MERC) significantly increased (Figure 5F). Additionally, the distance between mitochondria and ER membranes significantly decreased, and even direct contact between mitochondria and ER (Figure 5G). Through immunofluorescence double staining using markers for ER (IP3R1) and mitochondria (VDAC1), we observed a significant increase in co-localization of immunofluorescence signals upon knocking down S1P (Figure 5H). Furthermore, we conducted a proximity ligation assay (PLA) to further validate the increased contact between the ER and mitochondria after knocking down S1P (Figure 5I).

According to NGS data analysis, we observed enrichment of calcium-mediated signaling pathways and calcium-binding related pathways in NP cells after S1P knockdown (Supplemental Figure 4, C and D). The physiological activities and functions of the mitochondria and ER and are linked to calcium ion dynamics (Figure 6A). Consequently, we hypothesize that knocking down S1P affects intracellular calcium flux. As shown in Figure 6, B - D, NP cells in the physiological state exhibited relatively low levels of intracellular calcium ions, which moderately increased upon S1P knockdown. After induction with H_2O_2, there was a significant elevation in cytosolic calcium levels in NP cells, which was notably higher than both the NC group and the S1P siRNA group. Moreover, upon S1P knockdown and subsequent H_2O_2

induction, cytosolic calcium levels further rise, indicating a potentially heightened oxidative stress level (Figure 6B). The ER calcium levels in NP cells were relatively higher compared to cytoplasmic calcium levels, reflecting a physiological condition. However, upon S1P knockdown, ER calcium levels significantly increased. Previous studies have suggested that an increase in ER membrane content can expand the ER surface area, thereby enhancing its calcium storage capacity (26, 27). Thus, we hypothesized that the elevated ER calcium levels observed after S1P knockdown are due to ER expansion, resulting in enhanced calcium storage capacity. Upon H_2O_2 induction, the ER calcium levels in NP cells decreased, in accordance with prior research indicating that oxidative stress induced by H_2O_2 leaded to the opening of calcium channels on the ER membrane, promoting calcium efflux. Subsequently, following S1P knockdown and H_2O_2 induction, ER calcium levels within NP cells also significantly decreased (Figure 6C). Notably, the difference between the S1P knockdown and H_2O_2-induced groups is not significant, suggesting that the accumulated calcium in the ER following S1P knockdown was efficiently released in response to H_2O_2-induced oxidative stress. Despite a significant increase in mitochondrial calcium levels in S1P knockdown NP cells compared to the NC group, the absolute calcium levels within mitochondria remained relatively low. Upon H_2O_2 induction, mitochondrial calcium levels in NP cells significantly increased due to oxidative stress-induced calcium efflux from the ER into the mitochondria. Furthermore, after S1P knockdown and subsequent H_2O_2 induction, mitochondrial calcium levels significantly raised compared to the H_2O_2-induced group (Figure 6D).

Disrupted calcium flux leads to oxidative stress and mitochondrial dysfunction.

Elevated calcium signaling can activate enzymes producing reactive oxygen species (ROS) and generate free radicals (28). As depicted in Figure 7A, the percentages of ROS production in the S1P knockdown group, H_2O_2 treatment group, and S1P knockdown followed by H_2O_2 treatment group all exhibited significant increases. While the rise in ROS was relatively modest in the S1P knockdown group alone, with an approximate 11% increase compared to NC, it markedly escalated by 62% and 74% in the H_2O_2 treatment group and the S1P knockdown followed by H_2O_2 treatment group respectively. These trends aligned with our previously measured mitochondrial calcium ion levels. We further validated mitochondrial oxidative stress in nucleus pulposus cells using MitoSOX staining. NP cells in the NC group exhibited relatively weak MitoSOX fluorescence intensity, while the strongest MitoSOX fluorescence intensity was observed in NP cells of the S1P knockdown followed by H_2O_2 treatment group indicating a state of cellular stress (Figure 7B).

We then performed JC-1 experiment to assess mitochondrial membrane potential and observed that in the NC group, the majority of NP cells exhibited JC-1 staining concentrated in the Q1 and Q2 quadrants, indicating higher mitochondrial membrane potential (Figure 7C). However, upon H_2O_2 induction, particularly after S1P knockdown followed by H_2O_2 treatment, a significant decrease in mitochondrial membrane potential was observed. Additionally, we noted that in the NC group, S1P knockdown group, and H_2O_2-induced group, a subset of cells still clustered in the Q1 quadrant, suggesting the presence of NP cells with intact mitochondria. In contrast, in

353 the S1P knockdown followed by H_2O_2 induction group, only a few cells remained in
354 the Q1 quadrant, indicating a widespread reduction in mitochondrial membrane
355 potential in NP cells. We examined proteins associated with mitochondrial morphology
356 and found that the protein DRP1, which controls mitochondrial fission (29), was
357 significantly increased in the group S1P knockdown followed by H_2O_2 treatment.
358 Conversely, the protein MFN1, which controls mitochondrial outer membrane fusion
359 (30), was significantly reduced. This suggested that there was less mitochondrial fusion
360 and more fission in this group, ultimately leading to an increase in p16, p21, and p53 in
361 NP cells (Figure 7D) which are well-known senescence marker genes. Additionally,
362 electron microscopy revealed significant mitochondrial damage in the S1P knockdown
363 followed by H_2O_2 induction group (Supplemental Figure 5A).
364 Subsequent energy metabolism analysis revealed that the group with S1P knockdown
365 followed by H_2O_2 induction exhibited the lowest relative ATP content (Figure 7E).
366 Furthermore, the NADP+/NADPH ratio results indicated a weakened antioxidant
367 capacity in the S1P knockdown followed by H_2O_2 induction group (Figure 7F). To
368 further elucidate the impact of S1P knockdown on NP cell energy metabolism, we
369 employed the Seahorse XF-96 extracellular flux analyzer to measure the oxygen
370 consumption rate (OCR) and extracellular acidification rate (ECAR) of cells. As
371 illustrated in Figure 7, G and H, knocking down S1P significantly reduced the basal
372 respiration, respiratory chain coupling efficiency, and ATP production. Knocking down
373 S1P followed by H_2O_2 induction further decreased mitochondrial energy metabolism.
374 It is noteworthy that the proton leak phenomenon was significantly elevated in the S1P

knockdown group, indicating that from the onset of S1P knockdown, mitochondria in the cells had already started to experience damage, with the potential to induce aging in NP cells. Meanwhile, knocking down S1P followed by H_2O_2 significantly reduced the basal glycolytic rate, maximum glycolytic capacity and glycolytic reserve (Figure 7, I and J). Since NP cells are primarily glycolytic cells, this result indicated that knocking down S1P has an inhibitory effect on the energy metabolism of NP cells. Additionally, through NGS data analysis and GO enrichment, it was found that the pathways enriched in response to S1P knockdown were associated with aging (Supplemental Figure 5B). In summary, these data suggested that S1P knockdown exacerbated mitochondrial dysfunction and oxidative stress injury of NP cells, which revealed the mechanisms behind IVD aging caused by S1P deficiency.

The calcium channel inhibitor 2-APB or the drug combination of dasatinib and quercetin can rescue IVD degeneration and aging.

Considering the disruption of calcium flow from the ER to the mitochondria leading to mitochondrial dysfunction and eventually IVD aging, we conducted western blot experiments and found that knocking down S1P led to an increase in the expression of the calcium channel protein IP3R, while other channel proteins, GRP75 and VDAC1, showed no significant changes (Figure 8A). In the S1P knockdown followed by H_2O_2 induction, there was a slight decrease in the calcium channel proteins GRP75 and VDAC1, which we speculate may be related to negative regulation after calcium flow disruption in NP cells. The upregulation of the calcium channel IP3R to some extent contributes to the calcium influx from the ER to the mitochondria. We then used the

IP3R inhibitor, 2-aminoethoxydiphenyl borate (2-APB), to rescue NP cells subjected to S1P knockdown followed by H_2O_2 induction. Fortunately, the application of 2-APB effectively mitigated the degenerative phenotype observed in NP cells (Figure 8B). Additionally, the use of 2-APB to inhibit calcium ion channels also improved mitochondrial energy metabolism (Figure 8, C and D).

Furthermore, we employed dasatinib and quercetin (D + Q), a commonly used senolytic drug combination to reduce senescent cells (31). As illustrated in the schematic diagram (Figure 8E), we applied the D + Q treatment to naturally aging Acan-CreERT-S1P$^{f/f}$ mice at 15 months of age for a total of 10 weeks, with a weekly intraperitoneal injection. Our findings revealed that treatment with D + Q significantly reduced the presence of p16-immunopositive regions (Figure 8, F and G). Concurrently, treatment with D + Q aimed at eliminating senescent cells also exhibited a capacity to partially rescue the anabolism and catabolism of IVDs (Figure 8, F and H). suggesting its potential as a reliable therapeutic intervention for mitigating the aging effects resulting from S1P deficiency.

Discussion

IVD aging is a complex process influenced by a multitude of factors (32, 33). While previous studies have identified genetic mutations in S1P that result in developmental abnormalities (13, 14), its specific role within IVDs remains unexplored. In this study, we have demonstrated that the absence of S1P leads to disruptions in intracellular protein trafficking, resulting in ER distention and subsequent abnormal ER-mitochondrial calcium flux. This ultimately triggers mitochondrial oxidative stress and functional impairment, culminating in the manifestation of IVD aging and degeneration phenotypes (Graphical Abstract).

S1P is known to activate various transcription factors, such as ATF6 and SREBPs. ATF6 is involved in regulating the transcription of genes related to ER stress, unfolded protein response, autophagy, and apoptosis(11). SREBPs participate in the regulation of genes associated with lipid metabolism, inflammation, and autophagy (34). ER stress has been shown to affect the metabolism of extracellular matrix (ECM)-related proteins, thereby contributing to IVDD (35). However, we did not observe widespread and severe ER stress following the knockdown of S1P, and only the activity of ATF6 directly activated by S1P, as well as XBP-1, exhibited significant decreases. Interestingly, ATF6A and XBP-1 have both been shown in previous studies to participate in the COPII vesicle trafficking process (23–25) and we validated the impact of S1P knockdown on Sar1a and Sec23a. Notably, prior studies have indicated that Sec23a can be transcriptionally regulated by ATF6α, as referenced (24), which aligns with our findings. Sec23a functions in assembling cargo proteins from the ER into vesicles for transportation to

the Golgi apparatus. This process involves the recognition and binding of specific signal sequences on cargo proteins, in coordination with the Sec24 and Sec13/31 subunits, leading to the formation of the COPII complex (36). This complex envelops cargo proteins for transportation from the ER to the Golgi apparatus. Sar1a, on the other hand, plays a role in cargo protein recognition and formation of the COPII complex during vesicular transport (37). Sar1a stimulates the exchange of GDP for GTP on the ER membrane, inducing conformational changes and subsequent recruitment of the Sec23/24 heterodimer(38). NP cells require the synthesis and secretion of collagen and other extracellular matrix molecules to maintain the structure and function of IVDs. When vesicular transport is restricted, in line with our research findings, large molecular proteins such as collagen could become trapped within the ER, leading to functional disruption in NP cells.

In mitochondria, the homeostasis of calcium ions plays a crucial role in both cellular physiology and pathology. It controls the rate of energy production in mitochondria and promotes the generation of ROS (28). In the presence of superoxide, highly reactive hydroxyl radicals are formed within cells, leading to damage of cellular proteins, RNA, DNA, and lipids, and under sustained stimuli, this can lead to cellular senescence phenotypes (39). Studies have indicated that the accelerated aging of IVD is associated with increased ROS production. Moreover, the antioxidant levels in degenerated NP cells are reduced, making them more susceptible to oxidative damage (40, 41). Through JC-1 experiments, we observed the most significant decrease in mitochondrial membrane potential in cells with S1P knockdown and H_2O_2 induction. Considering the

calcium concentration gradient between the interior and exterior of mitochondria, the reduction in mitochondrial membrane potential can facilitate calcium influx. Moreover, the decrease in mitochondrial membrane potential can trigger the opening of the mitochondrial permeability transition pore (MPTP) (42), resulting in uncontrolled mitochondrial membrane permeability and calcium entry. Excessive calcium influx into mitochondria can also induce the opening of MPTP, leading to further reductions in mitochondrial membrane potential and increased ROS generation (43, 44). The increased calcium flow within mitochondria can be attributed to various factors. On one hand, as revealed in our research, we observed an increase in the expression of the calcium channel protein IP3R after S1P knockdown. On the other hand, previous studies have indicated that when the distance between the ER and mitochondria is 12-24 nm or shorter, direct calcium transfer through concentration gradients can occur (27, 45, 46). Given that S1P knockdown leads to ER expansion and elevated calcium storage levels, the combined effect of increased ER calcium storage, ER-mitochondria calcium exchange and direct calcium transfer, contributes to a significant increase in calcium influx into mitochondria upon H_2O_2 induction, leading to a profound reduction in mitochondrial membrane potential. The reduction in mitochondrial membrane potential is an irreversible event in the early stages of apoptosis, which can lead to the release of cytochrome C, activation of the caspase protein family, impairment of mitochondrial respiratory chain, and decreased energy metabolism (47, 48). Additionally, mitochondrial damage can further elevate intracellular oxidative stress levels, causing damage to mitochondrial DNA, impair the synthesis of mitochondrial proteins, and

inhibit mitochondrial respiration, thereby affecting normal mitochondrial function. Subsequently, this cascade of events can lead to mitochondrial apoptosis (49, 50), initiating a vicious cycle of events, ultimately, resulting in the appearance of senescence phenotypes in IVD (51). In summary, impaired mitochondrial calcium flux disrupts cellular calcium homeostasis, leading to increased ROS production from mitochondria. This oxidative stress, in turn, contributes to mitochondrial dysfunction, creating a feedback loop that exacerbates cellular damage and dysfunction IVD.

It is worth noting that knocking down S1P in the early stages (2 days) did not lead to a significant NP cell aging phenotype. We speculate that this might be because S1P's regulation of NP cell aging is not directly mediated through protein-protein interactions or transcriptional regulation. Our experiments collectively indicated that upon knocking down S1P, NP cells experienced ER swelling and accumulated more calcium ions. These calcium ions did not leak within the short term, thus not affecting cellular physiological functions. However, under other stress conditions, such as oxidative stress induced by H_2O_2, calcium ions within ER rapidly influxed into mitochondria, thereby exacerbating oxidative stress, inducing mitochondrial damage, and promoting NP cells aging eventually. Moreover, in vivo, with decreasing S1P expression during age process, various age-related stress factors emerge within the IVD, such as inflammatory stimuli and mechanical load. These factors further enhance S1P's influence on IVD aging. We observed that S1P knockout mice tend to exhibit aging phenotypes more readily at the same age under normal feeding conditions, which validating this hypothesis.

In conclusion, our study provides the first elucidation of the role of S1P in the IVD and demonstrates that the depletion of S1P leads to IVD aging through vesicular transport, ER-mitochondrial calcium flux, and oxidative stress pathways. In the treatment of IVD aging, rescuing the decrease in S1P expression could potentially mitigate the aging process caused by various stress factors within the IVD.

Materials and methods

Animals

Sex was not considered as a biological variable in this research. S1P flox/flox mice were generously supplied by Professor Di Wang from Zhejiang University. Shh-cre mice were a gift from An Qin from Shanghai Jiao Tong University. Acan-creERT mice were purchased from Gempharmatech. Acan-creERT mice were induced by continuous intraperitoneal injections of tamoxifen dissolved in corn oil (100 μg per gram of body weight) for five consecutive days at age of 8 weeks. Throughout all experiments, comparisons were made between the Shh-cre-$S1P^{f/f}$ or Acan-Cre-$S1P^{f/f}$ mice and their $S1P^{f/f}$ littermates.

Animal model

The needle-puncture degeneration model was carried out in wildtype mice at age of 12 weeks. The mice were divided into two groups randomly: one was the sham group (no disc puncture), and the other group involved using a 27-gauge needle to puncture the Co7/Co8 and Co8–Co9 IVDs to the center. After four weeks, the mice were sacrificed, and samples were collected (4 weeks post-puncture group). The tail-looping degeneration model was performed in Acan-creERT-$S1P^{f/f}$ mice and $S1P^{f/f}$ mice at the age of 12 weeks. Briefly, the tail of the mice was fixed at a specific location, positioned between vertebrae Co5 and Co13 using a 0.8-mm stainless steel wire to secure the loop in place, and the end portion of the tail was removed (52). This disc-compression model was designed to ensure consistent compression in all mice, minimizing surgical variability. Mice were euthanized at 8 weeks following the looping procedure for

histological assessment.

Immunohistochemistry and immunofluorescence

Human IVD samples were sourced from Sir Run Run Shaw Hospital, Zhejiang University School of Medicine. Patient characteristics are listed in Supplementary Table 1. The IVD sections or cell slides underwent immunohistochemical or Immunofluorescence staining. To block endogenous peroxidase activity, 3% H_2O_2 was applied for 10 minutes, succeeded by trypsin for 20 minutes, and then 5% BSA for 30 minutes to prevent non-specific antigen binding. Primary antibodies were left to incubate overnight at 4°C. On the subsequent day, sections were washed in PBS with 1% Tween and treated with corresponding HRP-conjugated secondary antibodies (Cell Signal Technology) for 1 hour at ambient temperature. Diaminobenzidine (DAB) was used for immunolabeling visualization, followed by hematoxylin counterstaining.

For Immunofluorescence staining, secondary antibodies labeled with Alexa Fluor 488 and/or 594 were applied for 1 hour at room temperature. The nucleus was stained using a 10 μg/mL solution of DAPI. Positively stained cells were quantified by assessing three randomly selected fields within the NP region, calculating the ratio of stained to total cells. Each specimen was sectioned at least three times, with data being averaged. Histological grading was used to evaluate cellular and morphological changes in both the annulus fibrosus (AF) and NP. Three independent and blinded investigators assessed the histological sections.

Cell transfection

SiRNA sequence targeting S1P was purchased from ThermoFisher, while siRNA

sequences targeting DNMT1, DNMT3a, and DNMT3b are provided in the Supplementary Table 2.

Human primary NP cells were plated in 6-well plates and cultured until reaching a cell confluence of 70% - 80%. siRNAs were transfected into the NP cells using Lipofectamine 3000 (Invitrogen, US). Transfection reagent including two tubes. In one tube, add 100μL of Opti-MEM and 2μg of siRNA per well. In the other tube, add 100μL of Opti-MEM and 5μL of Lipofectamine 3000 per well. Let the two tubes stand for 2 minutes each, then mix them together and incubate at room temperature for 15 minutes. After replacing the medium in the culture plate with fresh medium, add 200μL of the transfection mixture to each well. 2 days after transfections, the complete medium was exchanged for subculture.

Induction of NP cell senescence in vitro

Before inducing with H_2O_2, a Cell Counting Kit-8 (CCK-8) assay was conducted to determine the appropriate concentration (Supplemental Figure 1B). After confirming the healthy growth status of the passaged cells, cell culture plates were prepared according to the appropriate concentration determined through CCK8 assays for NP cells. To induce NP cells senescence, the cells were treated with 100 μm H_2O_2 for induction, with durations of 2 hours, 4 hours, and 6 hours. Following the designated H_2O_2 induction times, cells were washed twice with PBS and fresh culture medium was added for an additional 5 days of cultivation.

As for treatment groups, human NP cells were randomly allocated into four groups: NC group (transfected with control siRNA), si-S1P group (transfected with S1P siRNA),

573 H_2O_2 group (transfected with control siRNA for 2 days and treated with 100 μm H_2O_2
574 for 2 hours), and si-S1P + H_2O_2 group (transfected with S1P siRNA for 2 days and
575 treated with 100 μm H_2O_2 for 2 hours).

576 **MSP experiment**

577 The promoter sequence of the human S1P gene was acquired from the UCSC Genome
578 Bioinformatics website (http://genome.ucsc.edu/) by selecting the upstream 2000bp
579 region from the transcription start site. Subsequently, MSP primers were designed for
580 the S1P promoter sequence using the methylation prediction website
581 (http://www.urogene.org/methprimer/). The MSP primer sequences are listed in the
582 Supplementary table 4. One set of primers was designed for completely methylated
583 specific sequences, capable of detecting unmethylated cytosines that remained
584 unconverted during bisulfite treatment (hm S1P MSP M F/R). Another set of primers
585 was designed for completely unmethylated sequences, targeting cytosines that were
586 converted from unmethylated cytosines to uracils (hm S1P MSP U F/R). The PCR
587 products were subjected to 1% agarose gel electrophoresis, followed by visualization
588 using a UV gel imaging system.

589 **BSP experiment**

590 The promoter sequence of the S1P gene was submitted to the methylation prediction
591 website to obtain BSP primer sets (Supplementary table 4). DNA samples treated with
592 sodium bisulfite were subjected to PCR amplification using the BSP primer sets.
593 Subsequently, the purified PCR products were ligated into the pMD19-T plasmid vector
594 and transformed into competent bacteria. The bacteria were plated on agar plates and

incubated overnight. Then, ten randomly selected colonies were amplified, and the samples were sent for gene sequencing. The sequencing results were aligned with the predicted CpG island sequence to identify methylated and unmethylated sites. The percentage of methylated sites in the cloned fragments was calculated.

SA-β-galactosidase staining

After the experimental pretreatment of NP cells, remove the cell culture medium and wash with PBS twice. Add 1mL of β-galactosidase staining fixative solution to each well and incubate at room temperature for 15 minutes. After fixation, remove the fixative solution and wash the cells with PBS for 3 minutes, repeating for 3 times. After discarding PBS, add 1mL of β-galactosidase staining working solution to each well and incubate at 37°C overnight. After overnight incubation, remove the staining solution, wash with PBS for 3 minutes to remove excess staining solution, repeat 3 times. Observe under a standard light microscope and count the number of positively stained cells.

Cell cycle assay

The cell cycle distribution was assessed using the Cell Cycle Analysis Kit (Beyotime Biotech). To summarize, NP cells were collected, washed twice with cold PBS, and subsequently fixed in 70% ethanol at 4°C overnight. Subsequently, the cells were stained with a solution of PI and RNase A for 30 minutes at 37°C in the absence of light. Ultimately, The resulting cell cycle distributions were subsequently analyzed using flow cytometry (CytoFLEX) and interpreted with FlowJo V10 software to quantify the different cell cycle phases.

Quantitation of mitochondria–ER contacts (MERC)

MERC were determined based on regions with a distance less than 50 nm between the ER and the outer mitochondrial membrane (OMM) in transmission electron microscopy micrographs. Quantitative analysis involved assessing the length of MERC, and the mean distance less than 50 nm between ER and OMM within each MERC.

Duolink proximity ligation assay (PLA)

Duolink PLA (Sigma Aldrich) is a technique that allows for the detection, visualization, and quantification of protein interactions, typically at a scale of around 40 nm or less, as individual fluorescent dots under a microscope. Briefly, cells after treatment underwent permeabilization with 0.1% Triton X-100 and were subsequently incubated overnight at 4°C with primary antibodies (IP3R1 and VDAC1), Then the cells were washed with PBS containing 0.3% Tween and incubated with PLA probes. The ligation and polymerization steps were conducted in accordance with the manufacturer's recommendations from Sigma Aldrich. For analysis, at least 6 fields per group were acquired to count the dots and normalized them based on cell count with the BlobFinder software (Olink Bioscience).

Measurement of intracellular calcium ions

Intracellular Calcium ions were detected according the protocol (53). In brief, for cytoplasmic Ca^{2+} measurements, a 2.5 μM fluorescent Ca^{2+} indicator dye, Fluo-4AM (from Yeasen Biotech), was used and incubated at 37°C for 30 minutes. For ER Ca^{2+} measurements, ionomycin (10 μM) was employed to clear intracellular free calcium ions, after which Fluo-4AM was used for measurement. For mitochondrial Ca^{2+}

measurements, 2.5 μM Rhod-2 AM (Yeasen Biotech) was incubated at 37°C for 30 minutes. Finally, average fluorescence intensity was measured using flow cytometry (CytoFLEX).

Measurement of intracellular ROS production

To assess ROS levels in NP cells, we employed the 2,7-dichlorofluorescin diacetate (DCFH-DA) assay (Yeasen Biotech). After treatment of each group, the cells were rinsed with PBS. Subsequently, a 10 μM solution of DCFH-DA was introduced to the plates and allowed to incubate for an additional 30 minutes at 37°C. Following this, the cells were washed with PBS and subjected to analysis using flow cytometry (CytoFLEX, Beckman Coulter).

Mitochondrial membrane potential assay

Mitochondrial membrane potential assessment was performed using the JC-1 Assay Kit obtained from Yeasen Biotech, in accordance with the manufacturer's instructions. In summary, NP cells were plated in 24-well plates and exposed to JC-1 staining solution in the absence of light at 37°C for 20 minutes. Following staining, the cells underwent two PBS washes and subjected to analysis using flow cytometry (CytoFLEX). A total of 10,000 events were recorded during the flow cytometry process. At low mitochondrial membrane potential, JC-1 forms JC-1 monomer exhibiting green fluorescence, whereas the JC-1 aggregates show red fluorescence.

Seahorse metabolic profiling assays

Oxygen consumption rate (OCR) measurements were conducted employing the Seahorse XF96 Mito Stress Test Kit and the Seahorse XF96 Extracellular Flux

Bioanalyzer, both from Seahorse Bioscience. Following the treatment of each group, NP cells were seeded in XF96 Cell Culture miniplates, without phenol red. According to the protocol, this test involved the use of various compounds, including Oligomycin (an ATP-synthase inhibitor), FCCP (a mitochondria uncoupler, and the FCCP concentration was 1μM.), Rotenone (a complex I inhibitor), and Antimycin A (a cytochrome C reductase inhibitor), all of which were obtained from Sigma. These compounds were used to create a profile of ATP-linked respiration, maximal respiration, and non-mitochondrial respiration. To standardize the results according to cell quantity in each well, the obtained OCR data was subjected to normalization through the Seahorse software. To determine the cell numbers, CyQuant (Life Technologies) was employed, as per the manufacturer's guidelines. This quantification step was executed after the Seahorse measurements were concluded, directly on the Seahorse plate. The entire process was replicated three times at the biological level, and the measurements from these replicates were then merged for subsequent analysis.

Statistical Analysis

The data was presented as mean ± standard deviation (SD). Prism 8 software (GraphPad Software, Inc., San Diego, CA, USA) was utilized for data analysis. Student's t-test or one-way ANOVA, followed by Tukey's post hoc analysis, was employed to assess statistical significance. At least three separate experiments were conducted, yielding consistent outcomes and statistical significance was considered at $p < 0.05$.

Study approval

The patient samples used in this study were collected with informed consent from the

individuals and was approved by the Ethics Review committee of Sir Run Run Shaw Hospita. All animal model experiments adhered to the guidelines and protocols established in the National Institutes of Health Guide for the Care and Use of Laboratory Animals, as well as the animal treatment standards of Zhejiang University (No. 25986).

Data availability

The data analyzed to support the findings in this study are available from the Supporting data values. Additional data related to this paper are available from corresponding author upon request.

Acknowledgments

This research was supported by National Natural Science Foundation of China under Grant No.82202734, 82272521. Zhejiang Provincial Natural Science Foundation of China under Grant No. LZ23H060002, LGD22H060002. China Postdoctoral Science Foundation Special Grant No. 2021TQ0279. Zhejiang Medical Science and Technology Project under Grant No. 2023564481.

Address correspondence to: Fengdong Zhao, Department of Orthopaedic Surgery, Sir Run Run Shaw Hospital, Zhejiang University School of Medicine, Hangzhou, Zhejiang, 310027, China; CN. Phone:+86 13858120759; E-mail: zhaofengdong@zju.edu.cn.

Author contributions

B.Z. - Conceptualizing experiments, validation, investigations, data visualization, and writing. X.Z. – Investigations, methodology and editing. X.K - Literature search and classification and editing. J.L. - Review and editing. B.H. - Review and editing. H.L. -

Review and editing. Z.J - Review and editing. X.W. - Review and editing. S.T. - Review and editing. Z.S., Z.L. - Review and editing, J.L., J.C., F.Z. - Conceptualization, project administration, funding acquisition, review and editing.

Conflict of Interest Statement

The authors declare no competing interests.

References

1. Sambamoorthi U, Tan X, Deb A. Multiple chronic conditions and healthcare costs among adults. Expert Rev Pharmacoecon Outcomes Res. 2015;15(5):823–32.

2. Roberts S, Evans H, Trivedi J, Menage J. Histology and pathology of the human intervertebral disc. J Bone Joint Surg Am. 2006 Apr;88 Suppl 2:10–4.

3. Rodriguez AG, Rodriguez-Soto AE, Burghardt AJ, Berven S, Majumdar S, Lotz JC. Morphology of the human vertebral endplate. J Orthop Res Off Publ Orthop Res Soc. 2012 Feb;30(2):280–7.

4. Videman T, Battié MC, Gill K, Manninen H, Gibbons LE, Fisher LD. Magnetic resonance imaging findings and their relationships in the thoracic and lumbar spine. Insights into the etiopathogenesis of spinal degeneration. Spine. 1995 Apr 15;20(8):928–35.

5. Gower WE, Pedrini V. Age-Related Variations in Proteinpolysaccharides from Human Nucleus Pulposus, Annulus Fibrosus, and Costal Cartilage. JBJS. 1969 Sep;51(6):1154.

6. Cieza A, Causey K, Kamenov K, Hanson SW, Chatterji S, Vos T. Global estimates of the need for rehabilitation based on the Global Burden of Disease study 2019: a systematic analysis for the Global Burden of Disease Study 2019. Lancet Lond Engl. 2021 Dec 19;396(10267):2006–17.

7. Sakai J, Rawson RB, Espenshade PJ, Cheng D, Seegmiller AC, Goldstein JL, et al. Molecular identification of the sterol-regulated luminal protease that cleaves SREBPs and controls lipid composition of animal cells. Mol Cell. 1998 Oct;2(4):505–14.

8. Seidah NG, Mowla SJ, Hamelin J, Mamarbachi AM, Benjannet S, Touré BB, et al. Mammalian subtilisin/kexin isozyme SKI-1: A widely expressed proprotein convertase with a unique cleavage specificity and cellular localization. Proc Natl Acad Sci U S A. 1999 Feb 16;96(4):1321–6.

9. Espenshade PJ, Cheng D, Goldstein JL, Brown MS. Autocatalytic processing of site-1 protease removes propeptide and permits cleavage of sterol regulatory element-binding proteins. J Biol Chem. 1999 Aug 6;274(32):22795–804.

10. Zheng Z, Zhang X, Huang B, Liu J, Wei X, Shan Z, et al. Site-1 protease controls osteoclastogenesis by mediating LC3 transcription. Cell Death Differ. 2021 Jun;28(6):2001.

11. Ye J, Rawson RB, Komuro R, Chen X, Davé UP, Prywes R, et al. ER Stress Induces Cleavage of Membrane-Bound ATF6 by the Same Proteases that Process SREBPs. Mol Cell. 2000 Dec 1;6(6):1355–64.

12. Yang J, Goldstein JL, Hammer RE, Moon YA, Brown MS, Horton JD. Decreased lipid synthesis in livers of mice with disrupted Site-1 protease gene. Proc Natl Acad Sci U S A. 2001 Nov 20;98(24):13607–12.

13. Achilleos A, Huffman NT, Marcinkiewicyz E, Seidah NG, Chen Q, Dallas SL, et al. MBTPS1/SKI-1/S1P proprotein convertase is required for ECM signaling and axial elongation during somitogenesis and vertebral development†. Hum Mol Genet. 2015 May 15;24(10):2884–98.

14. Kondo Y, Fu J, Wang H, Hoover C, McDaniel JM, Steet R, et al. Site-1 protease deficiency causes human skeletal dysplasia due to defective inter-organelle protein trafficking. JCI Insight. 2018 Jul 26;3(14):e121596, 121596.

15. C LO, Ma B, L P, M S, G K. The hallmarks of aging. Cell. 2013;153(6). doi:10.1016/j.cell.2013.05.039.

16. Wh G, Mc J, Sh B, D M. Modification of ion channels and calcium homeostasis of basal forebrain neurons during aging. Behav Brain Res. 2000;115(2). doi:10.1016/s0166-4328(00)00260-6.

17. R L, Y S, Z L, H Y, S Z, K W, et al. Impaired calcium homeostasis via advanced glycation end products promotes apoptosis through endoplasmic reticulum stress in human nucleus pulposus cells and exacerbates intervertebral disc degeneration in rats. FEBS J. 2019;286(21). doi:10.1111/febs.14972.

18. Finkel T, Holbrook NJ. Oxidants, oxidative stress and the biology of ageing. Nature. 2000 Nov;408(6809):239–47.

19. K S, X J, J G, X Y, F G. Mitophagy in degenerative joint diseases. Autophagy. 2021;17(9). doi:10.1080/15548627.2020.1822097.

20. Cruickshanks HA, McBryan T, Nelson DM, Vanderkraats ND, Shah PP, van Tuyn J, et al. Senescent cells harbour features of the cancer epigenome. Nat Cell Biol. 2013 Dec;15(12):1495–506.

21. Bertolotti A, Zhang Y, Hendershot LM, Harding HP, Ron D. Dynamic interaction of BiP and ER stress transducers in the unfolded-protein response. Nat Cell Biol. 2000 Jun;2(6):326–32.

22. Hirsch I, Weiwad M, Prell E, Ferrari DM. ERp29 deficiency affects sensitivity to apoptosis via impairment of the ATF6-CHOP pathway of stress response. Apoptosis Int J Program Cell Death. 2014 May;19(5):801–15.

23. Saito A, Hino S ichiro, Murakami T, Kanemoto S, Kondo S, Saitoh M, et al. Regulation of endoplasmic reticulum stress response by a BBF2H7-mediated Sec23a pathway is essential for chondrogenesis. Nat Cell Biol. 2009 Oct;11(10):1197–204.

24. Sriburi R, Jackowski S, Mori K, Brewer JW. XBP1: a link between the unfolded protein response, lipid biosynthesis, and biogenesis of the endoplasmic reticulum. J Cell Biol. 2004 Oct 11;167(1):35–41.

25. Liu L, Cai J, Wang H, Liang X, Zhou Q, Ding C, et al. Coupling of COPII vesicle trafficking to nutrient availability by the IRE1α-XBP1s axis. Proc Natl Acad Sci. 2019 Jun 11;116(24):11776–85.

26. Berridge MJ. The endoplasmic reticulum: a multifunctional signaling organelle. Cell Calcium. 2002 Nov 1;32(5):235–49.

27. Csordás G, Renken C, Várnai P, Walter L, Weaver D, Buttle KF, et al. Structural and functional features and significance of the physical linkage between ER and mitochondria. J Cell Biol. 2006 Sep 18;174(7):915–21.

28. Gordeeva AV, Zvyagilskaya RA, Labas YA. Cross-talk between reactive oxygen species and calcium in living cells. Biochem Biokhimiia. 2003 Oct;68(10):1077–80.

29. Serasinghe MN, Weider SY, Renault TT, Elkholi R, Asciolla JJ, Yao JL, et al. Mitochondrial division is requisite to RAS-induced transformation and targeted by oncogenic MAPK pathway inhibitors. Mol Cell. 2015 Feb 5;57(3):521–36.

30. Chen H, Detmer SA, Ewald AJ, Griffin EE, Fraser SE, Chan DC. Mitofusins Mfn1 and Mfn2 coordinately regulate mitochondrial fusion and are essential for embryonic development. J Cell Biol. 2003 Jan 20;160(2):189–200.

31. Novais EJ, Tran VA, Johnston SN, Darris KR, Roupas AJ, Sessions GA, et al. Long-term treatment with senolytic drugs Dasatinib and Quercetin ameliorates age-dependent intervertebral disc degeneration in mice. Nat Commun. 2021 Sep 3;12:5213.

32. Patil P, Dong Q, Wang D, Chang J, Wiley C, Demaria M, et al. Systemic clearance of p16INK4a-positive senescent cells mitigates age-associated intervertebral disc degeneration. Aging Cell. 2019;18(3):e12927.

33. Che H, Li J, Li Y, Ma C, Liu H, Qin J, et al. p16 deficiency attenuates intervertebral disc degeneration by adjusting oxidative stress and nucleus pulposus cell cycle. eLife. 2020 Mar 3;9:e52570.

34. Wang X, Sato R, Brown MS, Hua X, Goldstein JL. SREBP-1, a membrane-bound transcription factor released by sterol-regulated proteolysis. Cell. 1994 Apr 8;77(1):53–62.

35. Ito S, Nagata K. Roles of the endoplasmic reticulum-resident, collagen-specific molecular chaperone Hsp47 in vertebrate cells and human disease. J Biol Chem. 2019 Feb 8;294(6):2133–41.

36. King R, Lin Z, Balbin-Cuesta G, Myers G, Friedman A, Zhu G, et al. SEC23A rescues SEC23B-deficient congenital dyserythropoietic anemia type II. Sci Adv. 7(48):eabj5293.

37. Barlowe C, d'Enfert C, Schekman R. Purification and characterization of SAR1p, a small GTP-binding protein required for transport vesicle formation from the endoplasmic reticulum. J Biol Chem. 1993 Jan 15;268(2):873–9.

38. Zanetti G, Pahuja KB, Studer S, Shim S, Schekman R. COPII and the regulation of protein sorting in mammals. Nat Cell Biol. 2011 Dec 22;14(1):20–8.

39. Holmström KM, Finkel T. Cellular mechanisms and physiological consequences of redox-dependent signalling. Nat Rev Mol Cell Biol. 2014 Jun;15(6):411–21.

40. Ding F, Shao Z wu, Xiong L ming. Cell death in intervertebral disc degeneration. Apoptosis Int J Program Cell Death. 2013 Jul;18(7):777–85.

41. Kepler CK, Ponnappan RK, Tannoury CA, Risbud MV, Anderson DG. The molecular basis of intervertebral disc degeneration. Spine J Off J North Am Spine Soc. 2013 Mar;13(3):318–30.

42. Rao SP, Sharma N, Kalivendi SV. Embelin averts MPTP-induced dysfunction in mitochondrial bioenergetics and biogenesis via activation of SIRT1. Biochim Biophys Acta Bioenerg. 2020 Mar 1;1861(3):148157.

43. Berridge MJ. Calcium signalling remodelling and disease. Biochem Soc Trans. 2012 Apr;40(2):297–309.

44. Bauer TM, Murphy E. Role of Mitochondrial Calcium and the Permeability Transition Pore in Regulating Cell Death. Circ Res. 2020 Jan 17;126(2):280–93.

45. Nunes P, Cornut D, Bochet V, Hasler U, Oh-Hora M, Waldburger JM, et al. STIM1 juxtaposes ER to phagosomes, generating Ca^{2+} hotspots that boost phagocytosis. Curr Biol CB. 2012 Nov 6;22(21):1990–7.

46. Kar P, Parekh AB. Distinct spatial Ca2+ signatures selectively activate different NFAT transcription factor isoforms. Mol Cell. 2015 Apr 16;58(2):232–43.

47. Harman D. Aging: a theory based on free radical and radiation chemistry. J Gerontol. 1956 Jul;11(3):298–300.

48. Jones DP. Redox theory of aging. Redox Biol. 2015 Aug;5:71–9.

49. Shadel GS, Horvath TL. Mitochondrial ROS signaling in organismal homeostasis. Cell. 2015 Oct 22;163(3):560–9.

50. Zorov DB, Juhaszova M, Sollott SJ. Mitochondrial reactive oxygen species (ROS) and ROS-induced ROS release. Physiol Rev. 2014 Jul;94(3):909–50.

51. Chen B, Zhu R, Hu H, Zhan M, Wang T, Huang F, et al. Elimination of Senescent Cells by Senolytics Facilitates Bony Endplate Microvessel Formation and Mitigates Disc Degeneration in Aged Mice. Front Cell Dev Biol. 2022;10:853688.

52. Sakai D, Nishimura K, Tanaka M, Nakajima D, Grad S, Alini M, et al. Migration of bone marrow–derived cells for endogenous repair in a new tail-looping disc degeneration model in the mouse: a pilot study. Spine J. 2015 Jun 1;15(6):1356–65.

53. Zhang L, Li L, Leavesley HW, Zhang X, Borowitz JL, Isom GE. Cyanide-Induced Apoptosis of Dopaminergic Cells Is Promoted by BNIP3 and Bax Modulation of Endoplasmic Reticulum-Mitochondrial Ca2+ Levels. J Pharmacol Exp Ther. 2010 Jan;332(1):97–105.

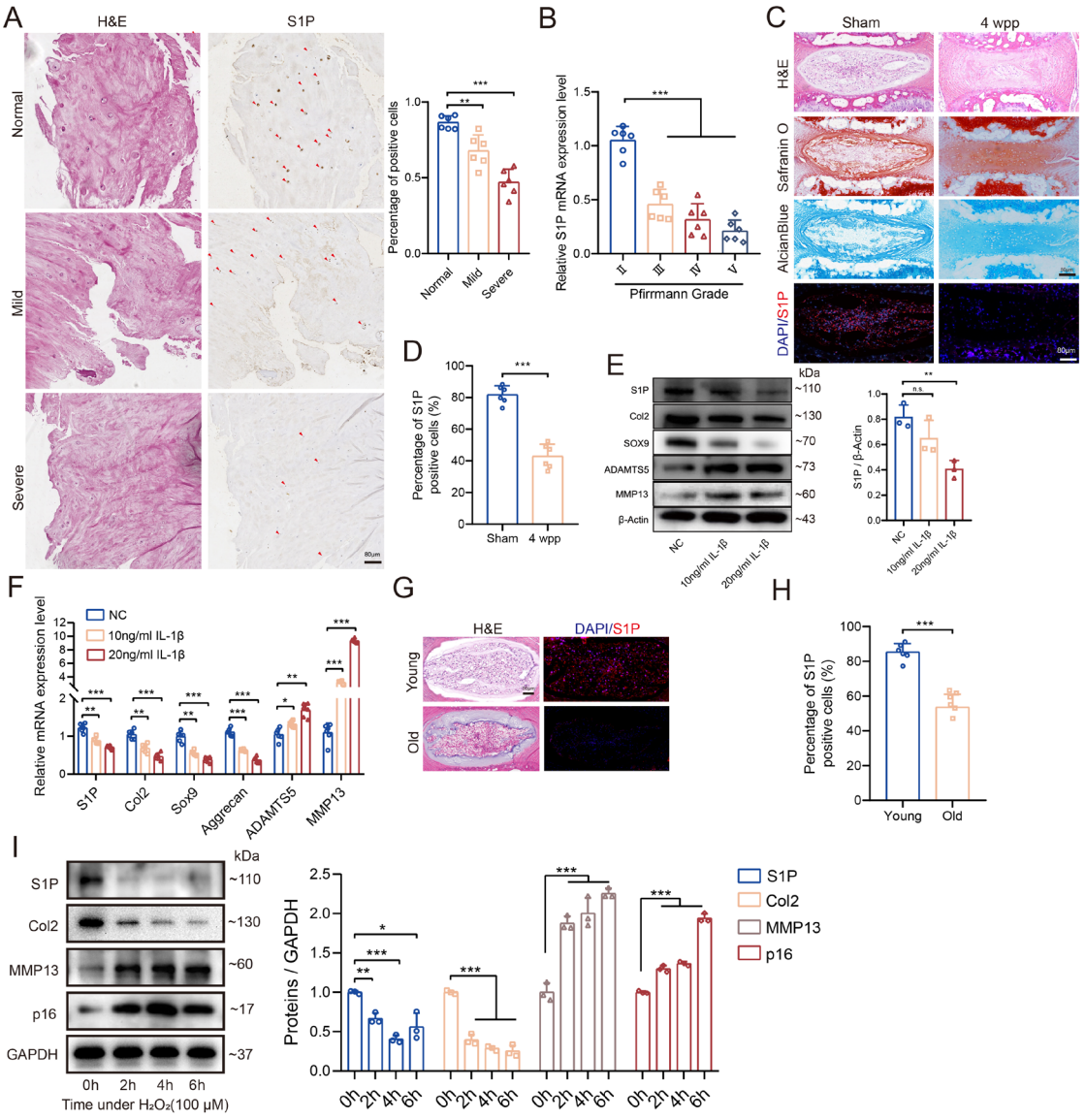

Figure 1

The expression of S1P in degenerated and aging IVD.

(A) Immunohistochemistry to detect S1P expression in normal, mild and sever degenerative IVD tissues and percentage of $S1P^+$ cells in IVD (n = 6, each group. ** $p < 0.01$, *** $p < 0.001$ compared with normal group. Scale bar: 80 μm). **(B)** qPCR analysis of S1P gene expression levels in NP tissue from IVDs with different Pfirrmann degeneration grades (n = 6, each group. *** $p < 0.001$ compared with Pfirrmann II grade). **(C)** Representative images displaying Safranin O, Alcian Blue, and S1P immunofluorescence staining in the sham group and the 4 weeks post-punctured group (4 wpp). Scale bars: 80 μm. **(D)** Percentage of $S1P^+$ cells in sham and 4 wpp group (n = 6, each group. *** $p < 0.001$ compared with sham group). **(E)** Immunoblots depicting the expression of S1P, Col2, SOX9, ADAMTS5, and MMP13 in human NP cells exposed to IL-1β at concentrations of 10 ng/ml or 20 ng/ml for 48 h and the quantification of the blot (n = 3, each group. ** $p < 0.01$, n.s = no significant compared with NC group). **(F)** Relative gene expression treated with IL-1β at concentrations of 10 ng/ml or 20 ng/ml for 48 h detected by qPCR (n = 6, each group. * $p < 0.05$, ** $p < 0.01$, *** $p < 0.001$ compared with NC group). **(G)** Representative immunofluorescence images of S1P in young (6 weeks old) and aged (24 months old) mice. Scale bars: 80 μm **(H)** Statistical analysis of the

871 percentage of S1P-positive cells (n = 6, each group. *** $p < 0.001$ compared with young group). **(I)**
872 Immunoblots of S1P, Col2, MMP13 and p16 in human NP cells after treatment with H_2O_2 for
873 different time intervals, along with their quantitative analysis (n = 3, each group. * $p < 0.05$, ** $p <$
874 0.01, *** $p < 0.001$ compared with 0 h group). Results are shown as points with means ± SD.
875 Student's t-test or one-way ANOVA, followed by Tukey's post hoc analysis, was employed to assess
876 statistical significance.
877

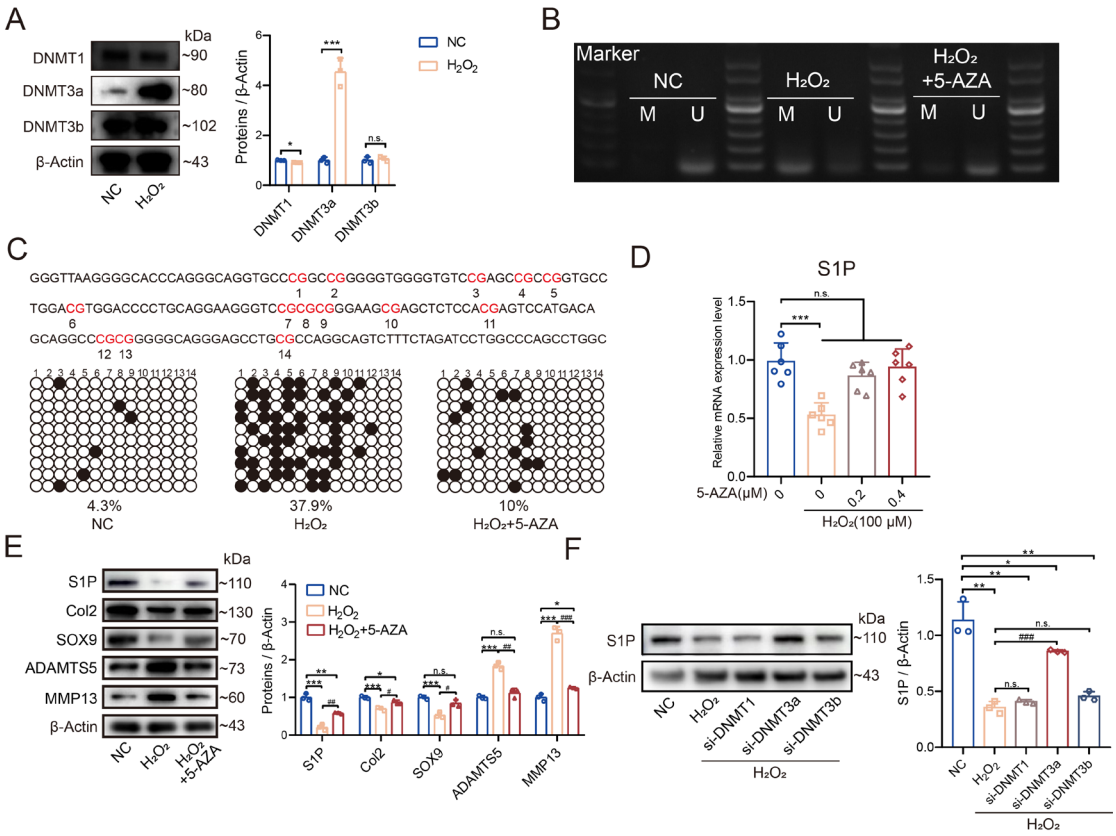

878
879 **Figure 2**

880 **The expression of S1P is regulated by DNA methylation.**

881 **(A)** Immunoblots showing the expression of methyltransferases in human NP cells after H_2O_2
882 treatment and the quantification of the blot (n = 3, each group. * $p < 0.05$, *** $p < 0.001$, n.s = no
883 significant compared with NC group). **(B)** Methylation-specific PCR (MSP) of the S1P promoter
884 region performed on NP cells treated with H_2O_2 (100 μM) and rescued with 5-AZA (0.2 μM). M
885 represented the methylated form of S1P, and U represented the unmethylated form of S1P. **(C)**
886 Bisulfite-specific PCR (BSP) sequencing detecting the s1p promoter region. The CpG islands were
887 highlighted in red within the sequenced PCR region. White and black circles represent unmethylated
888 and methylated CpG islands in the S1P promoter region of human NP cells treated with H_2O_2 (100
889 μM) and those rescued with 5-AZA (0.2 μM). Different rows within each group represent ten
890 bacterial monoclonals selected for sequencing in their respective groups. **(D)** qPCR analysis of S1P
891 treated with H_2O_2 (100 μM) and those rescued with different concentration of 5-AZA (n = 6, each
892 group. *** $p < 0.001$, n.s = no significant). **(E)** The protein expression levels and their quantification
893 of S1P, Col2, SOX9, ADAMTS5 and MMP13 in NP cells treated with H_2O_2 and those rescued 5-
894 AZA (n = 3, each group. * $p < 0.05$, *** $p < 0.001$, n.s = no significant compared with NC group. #
895 $p < 0.05$, ## $p < 0.01$, ### $p < 0.001$ compared with H_2O_2 group). **(F)** The protein expression levels
896 of S1P in Western blot treated with H_2O_2, DNMT1, DNMT3a and DNMT3b knockdown by siRNA
897 following H_2O_2 treatment and quantification of the blot (n = 3, each group. * $p < 0.05$, ** $p < 0.01$
898 compared with NC group. ### $p < 0.001$ compared with H_2O_2 group, n.s = no significant). Results
899 are shown as points with means ± SD. Student's t-test or one-way ANOVA, followed by Tukey's
900 post hoc analysis, was employed to assess statistical significance
901

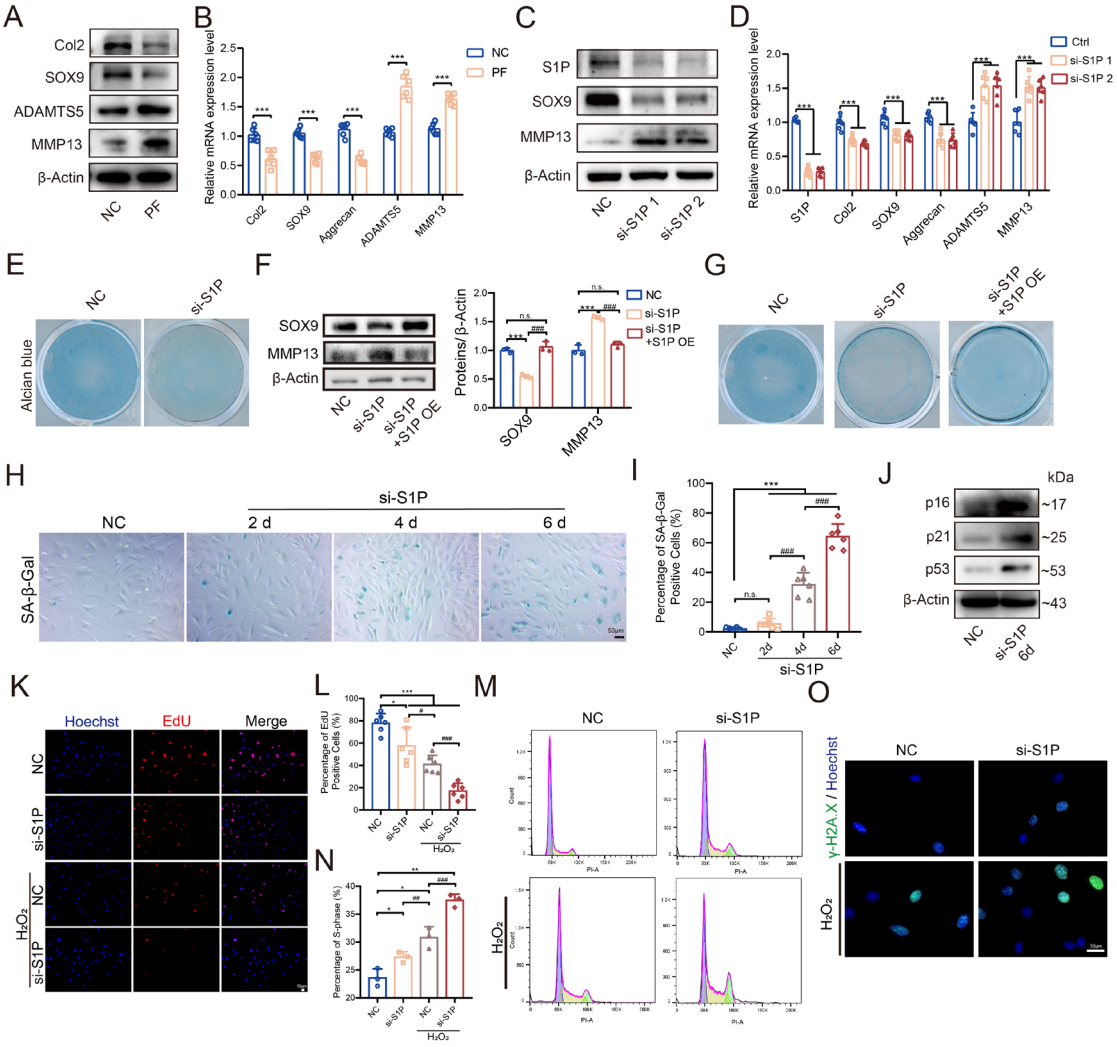

Figure 3

S1P deficiency leads to IVD degeneration and aging.

(A) Immunoblots showing the genes expression in NP cells treated with S1P inhibitor PF. **(B)** qPCR analysis for these genes treated with PF (n = 6, each group). **(C)** Immunoblots showing genes expression in NP cells after siRNA-mediated S1P knockdown. **(D)** qPCR analysis for genes expression after S1P knockdown (n = 6, each group). *** $p < 0.001$ compared with NC group. **(E)** Alcian Blue staining images of NP cells after S1P knockdown. **(F)** Immunoblots showing genes expression after S1P knockdown and rescue by S1P overexpression (OE) along with quantification of the blot (n = 3, each group. *** $p < 0.001$, n.s = no significant compared with NC group. ### $p < 0.001$ compared with si-S1P group). **(G)** Representative Alcian Blue staining images of NP cells after S1P knockdown and rescue by S1P OE. **(H)** SA-β-galactosidase (SA-β-Gal) staining images of NP cells after S1P knockdown and continued cultivation for different days. **(I)** Percentage of SA-β-Gal positive cells (n = 6, each group. *** $p < 0.001$, n.s = no significant compared with NC group. ### $p < 0.001$ compared with 4d group). **(J)** Immunoblots showing the expression of p16, p21 and p53 after S1P knockdown and continued cultivation for 6 days. **(K)** EdU staining and nuclei labeled with Hoechst of four groups: NC, si-S1P, NC + H_2O_2 and si-S1P + H_2O_2 group. **(L)** Percentage of EdU positive cells (n = 6, each group. * $p < 0.05$, *** $p < 0.001$ compared with NC group. # $p < 0.05$, ### $p < 0.001$ compared with NC + H_2O_2 group). **(M)** Cell cycle analysis by flow cytometry

measurement of four groups. G0/G1 phase (Purple region), the S phase (Yellow region), and the G2 phase (Green region). **(N)** Percentage of S phase (n = 3, each group. * $p < 0.05$, ** $p < 0.01$ compared with NC group. ## $p < 0.01$, ### $p < 0.001$ compared with NC + H_2O_2 group). **(O)** Representative immunofluorescence images of γ-H2A.X. Scar bars: 50 μm. Results are shown as means ± SD. Student's t-test or one-way ANOVA, followed by Tukey's post hoc analysis, was employed to assess statistical significance.

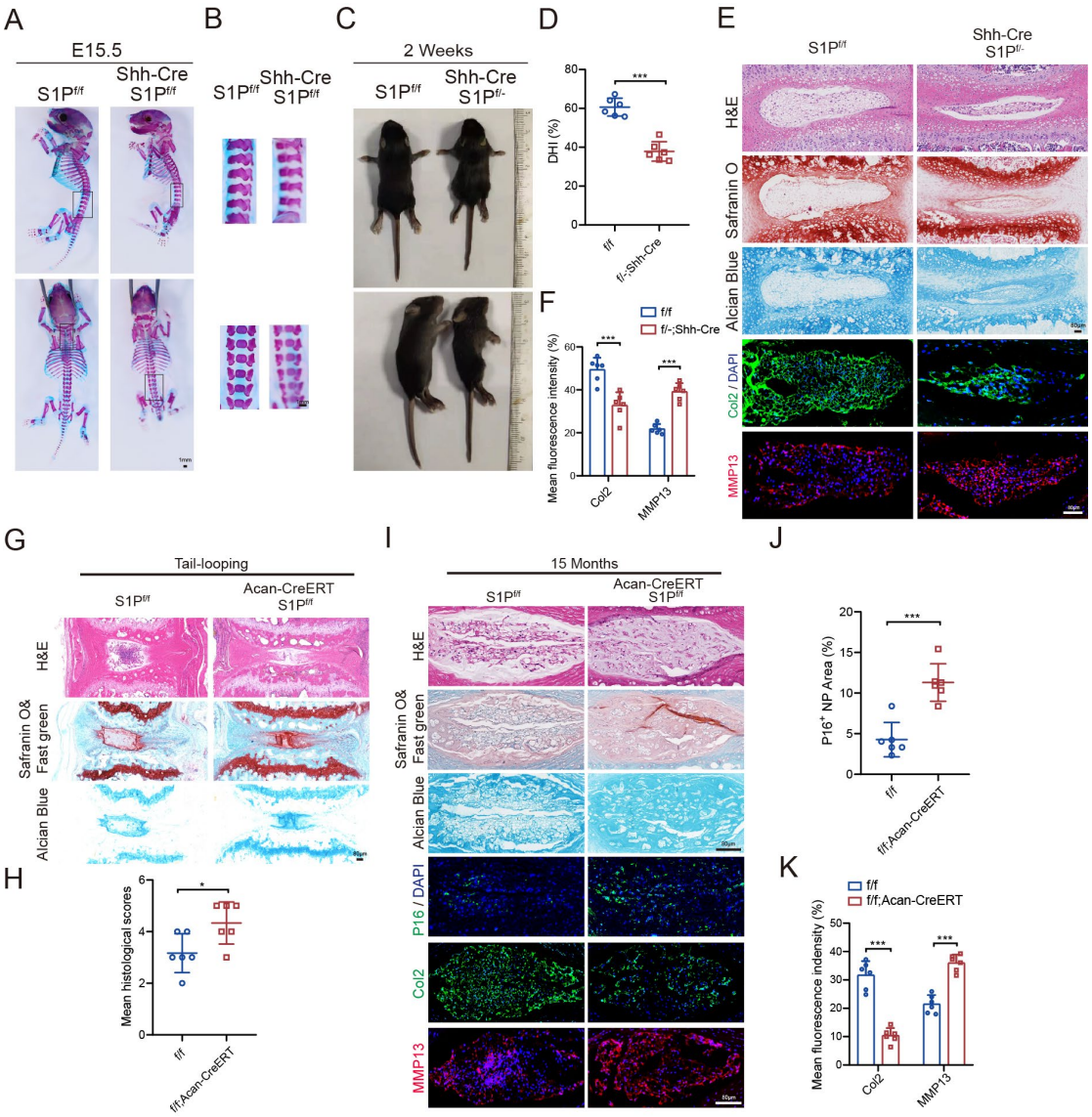

Figure 4

S1P conditional knockout mice exhibit a higher propensity for degeneration and aging.

(A) Double-stained images of S1P$^{f/f}$ and Shh-cre-S1P$^{f/f}$ embryonic mice at E15.5 days and **(B)** enlarged images of the spinal region within the black frame (stained with Safranin O in red for bone and Alcian Blue in blue for cartilage. Scar bar: 1 mm). **(C)** Images of 2-week-old S1P$^{f/f}$ and Shh-cre-S1P$^{f/-}$ mice. **(D)** Statistical analysis of percentage of the IVD height index (DHI) for S1P$^{f/f}$ and Shh-cre-S1P$^{f/-}$ mice (n = 6, each group) **(E)** Images of H&E, Safranin O, and Alcian Blue staining of IVD tissues from 2-week-old S1P$^{f/f}$ and Shh-cre-S1P$^{f/-}$ mice, as well as immunofluorescence images showing Col2 (Green) and MMP13 (Red) with DAPI staining for cell nuclei (Blue). **(F)** Mean fluorescence intensity for Col2 and MMP13 of 2-week-old S1P$^{f/f}$ and Shh-cre-S1P$^{f/-}$ mice (n = 6, each group). **(G)** H&E, Safranin O & Fast Green, and Alcian Blue staining images of IVD tissues from 12-week-old S1P$^{f/f}$ and Acan-creERT-S1P$^{f/f}$ mice after tail-looping modeling for 8 weeks. **(H)** Statistical analysis of the mean histological scores (n=6, each group). **(I)** Images of H&E, Safranin O & Fast Green, and Alcian Blue staining of IVD from 15-month-old naturally aging S1P$^{f/f}$ and Acan-creERT-S1P$^{f/f}$ mice, as well as immunofluorescence images showing p16, Col2, and MMP13. **(J)** Percentage of p16^{+} area (n = 6, each group). **(K)** Mean fluorescence intensity for Col2

and MMP13 (n = 6, each group). Scar bars: 80 μm. Results are shown as points with means ± SD. * $p < 0.05$, *** $p < 0.001$ compared with $S1P^{f/f}$ mice. Student's t-test or one-way ANOVA, followed by Tukey's post hoc analysis, was employed to assess statistical significance.

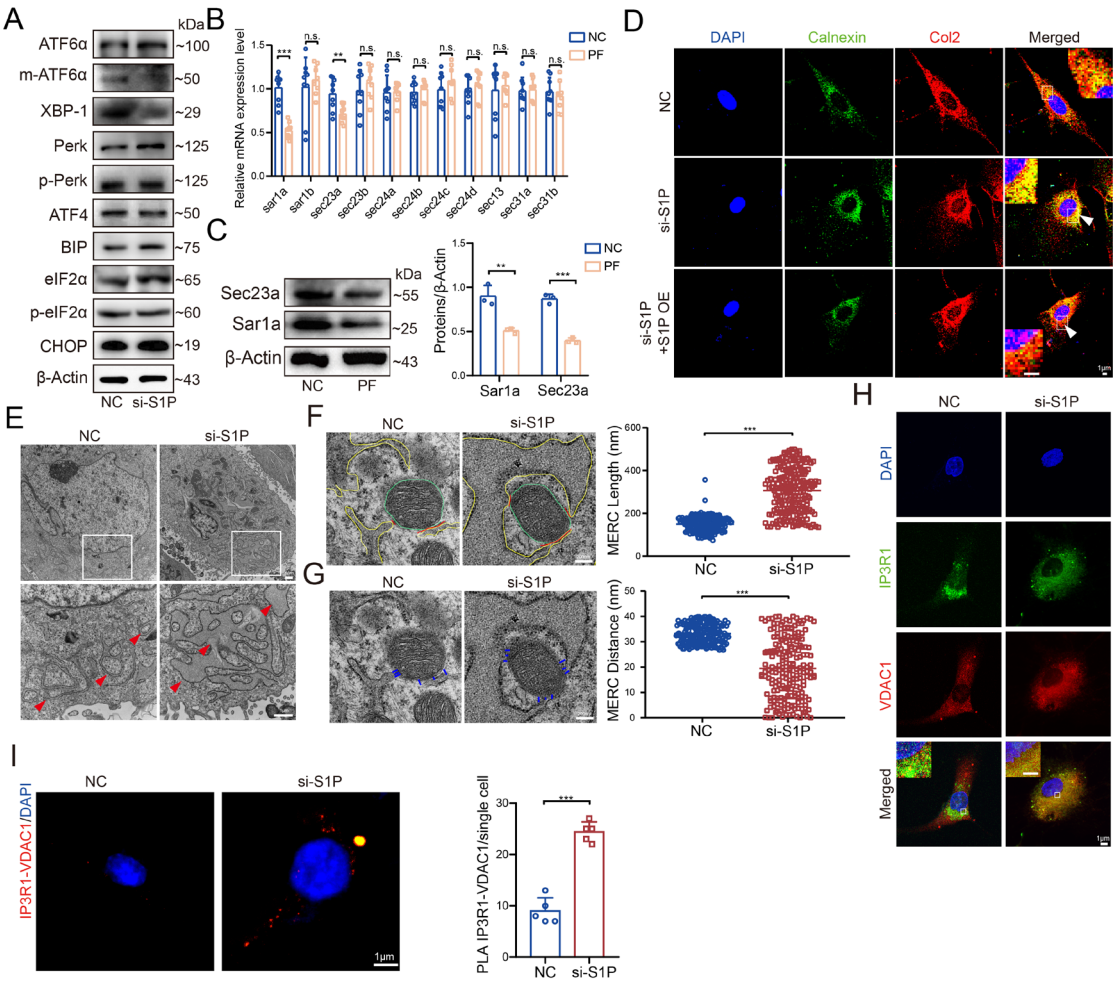

Figure 5

S1P deficiency affects ER state and ER-mitochondria associated contacts.

(A) Immunoblots depicting the genes expression related to ER stress in NP cells after S1P knockdown. **(B)** qPCR analysis for COPII-related gene expression. **(C)** Immunoblots depicting expression of Sec23a and Sar1a and quantification of the blot in NP cells treated with S1P inhibitor PF (n = 3, each group). The Sar1a blot provided were same samples and run contemporaneously. **(D)** Confocal immunofluorescence images of ER marker protein (Calnexin, green) and collagen protein (Col2, red) after S1P knockdown and rescue by S1P OE (White arrows indicate the yellow co-localization area). Scar bar: 1 μm. **(E)** Transmission electron microscopy (TEM) images depicting the ER state after S1P knockdown. Scar bar: 1 μm. **(F)** TEM images showing mitochondria-ER membrane contacts (MERC), with the yellow line representing the ER membrane, the green line indicating the mitochondrial membrane, and the red line indicating length of MERC less than 50 nm between mitochondria and ER (Scar bar: 200 nm), as well as the statistical analysis of MERC length (n = 200, each group). **(G)** TEM images showing MERC, with blue line indicating distance of MERC less than 50 nm between mitochondria and ER (Scar bar: 200 nm), as well as the statistical analysis of MERC distance (n = 200, each group). **(H)** Confocal immunofluorescence images of ER marker (IP3R1, red) and mitochondrial marker (VDAC1) after S1P knockdown. Scar bar: 1 μm. **(I)** Duolink proximity ligation assay (PLA) images of IP3R1-VDAC1 contact points and the statistical analysis of contact points / single cell after S1P knockdown (n = 6, each group). Scar bar: 1 μm. Results are shown as means ± SD. ** $p < 0.01$, *** $p < 0.001$, n.s = no significant

compared with NC group. ### $p < 0.001$ compared with NC + H_2O_2 group. Student's t-test or one-way ANOVA, followed by Tukey's post hoc analysis, was employed to assess statistical significance.

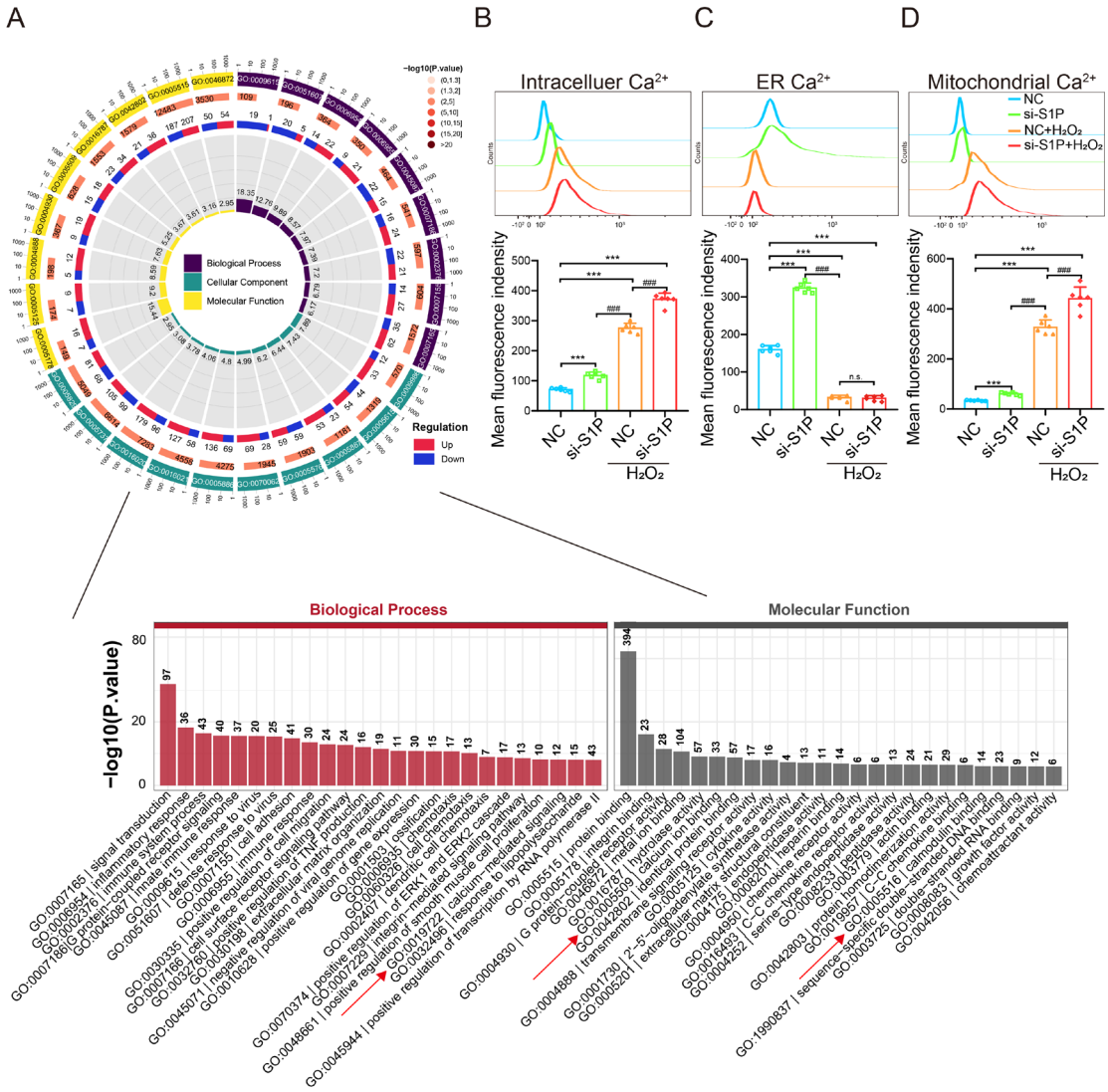

973

974 **Figure 6**

975 **S1P deficiency affects calcium ion homeostasis in NP cells.**

976 **(A)** Next-generation gene sequencing (NGS) analysis of gene ontology (GO) pathways, with red
977 arrows indicating the enriched calcium-related pathways. **(B)** Flow cytometry analysis of
978 cytoplasmic calcium ions, **(C)** ER calcium ions and **(D)** mitochondrial calcium ions, as well as
979 statistical analysis of mean fluorescence intensity to represent calcium ion concentration of four
980 groups. Results are shown as means ± SD, *** $p < 0.001$, n.s = no significant compared with NC
981 group. ### $p < 0.001$ compared with NC + H_2O_2 group. Student's t-test or one-way ANOVA,
982 followed by Tukey's post hoc analysis, was employed to assess statistical significance.

983

984

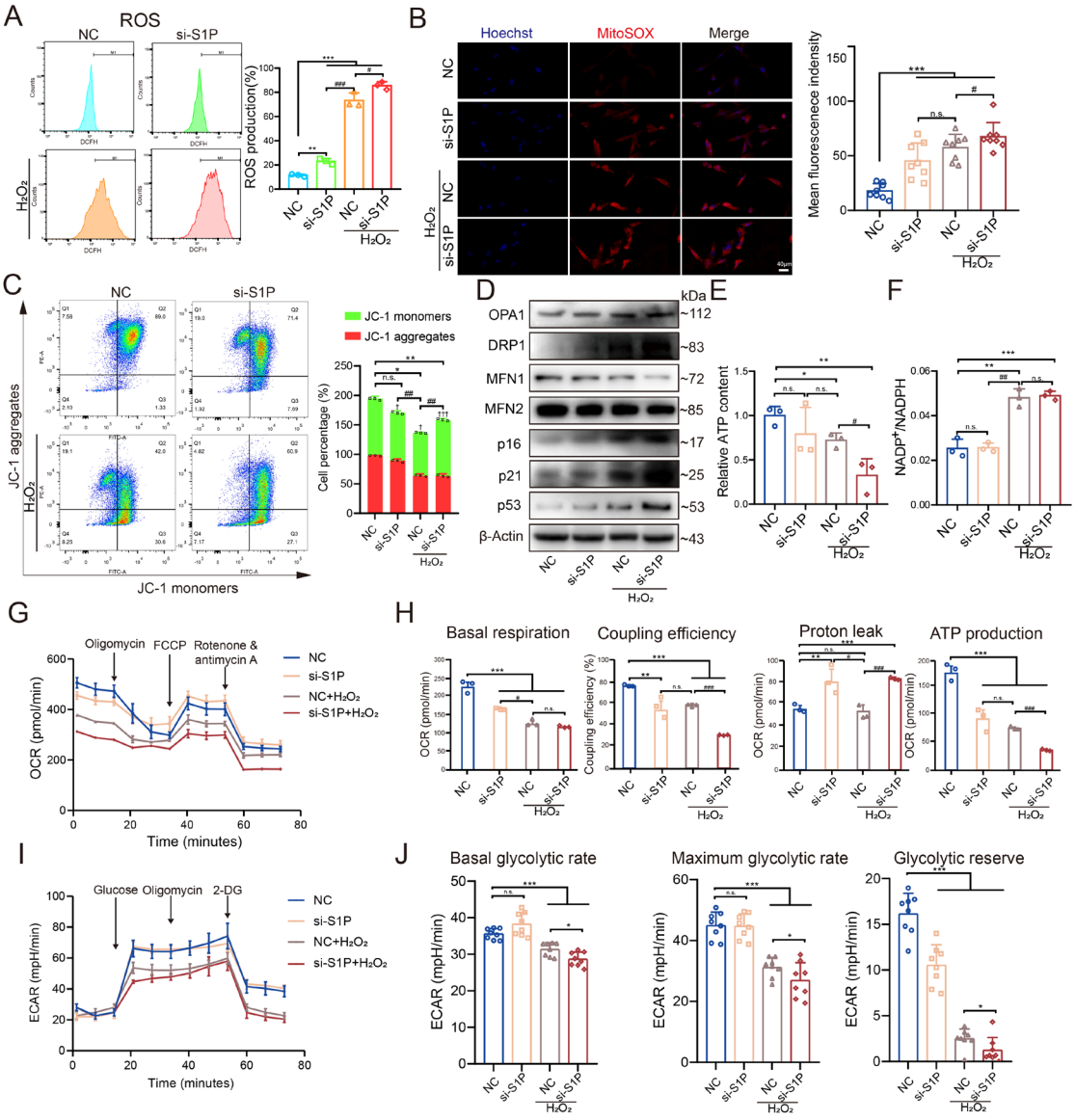

Figure 7

S1P deficiency affects mitochondrial function and energy metabolism.

(A) Flow cytometry analysis of ROS levels and the statistical assessment of ROS production of four groups (n = 3, each group). **(B)** MitoSOX fluorescence images and the analysis of mean fluorescence intensity of four groups (n = 8, each group). Scar bar: 40 μm. **(C)** JC-1 staining for mitochondrial membrane potential (n = 3, each group), where green represents JC-1 monomers indicating low potential, and red represents JC-1 aggregates indicating high potential. * $p < 0.05$, ** $p < 0.01$, n.s = no significant compared with NC group. ## $p < 0.01$ compared with NC + H_2O_2 group. † $p < 0.05$, ††† $p < 0.001$ compared with JC-1 monomers and JC-1 aggregates. **(D)** Immunoblots depicting the expression of OPA1, DRP1, MFN1and MFN2 as well as p16, p21, p53. **(E)** Relative ATP content of four groups (n = 3, each group). **(F)** The ratio of $NADP^+$ / NADPH of four groups (n = 3, each group). **(G)** Measurement of oxygen consumption rate (OCR) by seahorse experiment of four groups (n = 3, each group). **(H)** Statistical analysis of Seahorse experiment data, including basal respiration, maximal respiration, non-mitochondrial oxygen consumption, coupling efficiency, proton leak, and ATP production. **(I)** Measurement of extracellular acidification rate (ECAR) by seahorse experiment of four groups (n = 8, each group). **(J)** Statistical analysis of Seahorse experiment data, including

basal glycoltic rate, maximum glycolytic rate and glycolytic reserve. Results are shown as means ± SD. * $p < 0.05$, ** $p < 0.01$, *** $p < 0.001$ compared with NC group. # $p < 0.05$, ## $p < 0.01$, ### $p < 0.001$ compared with NC + H_2O_2 group, n.s = no significant. Student's t-test or one/two-way ANOVA, followed by Tukey's post hoc analysis, was employed to assess statistical significance.

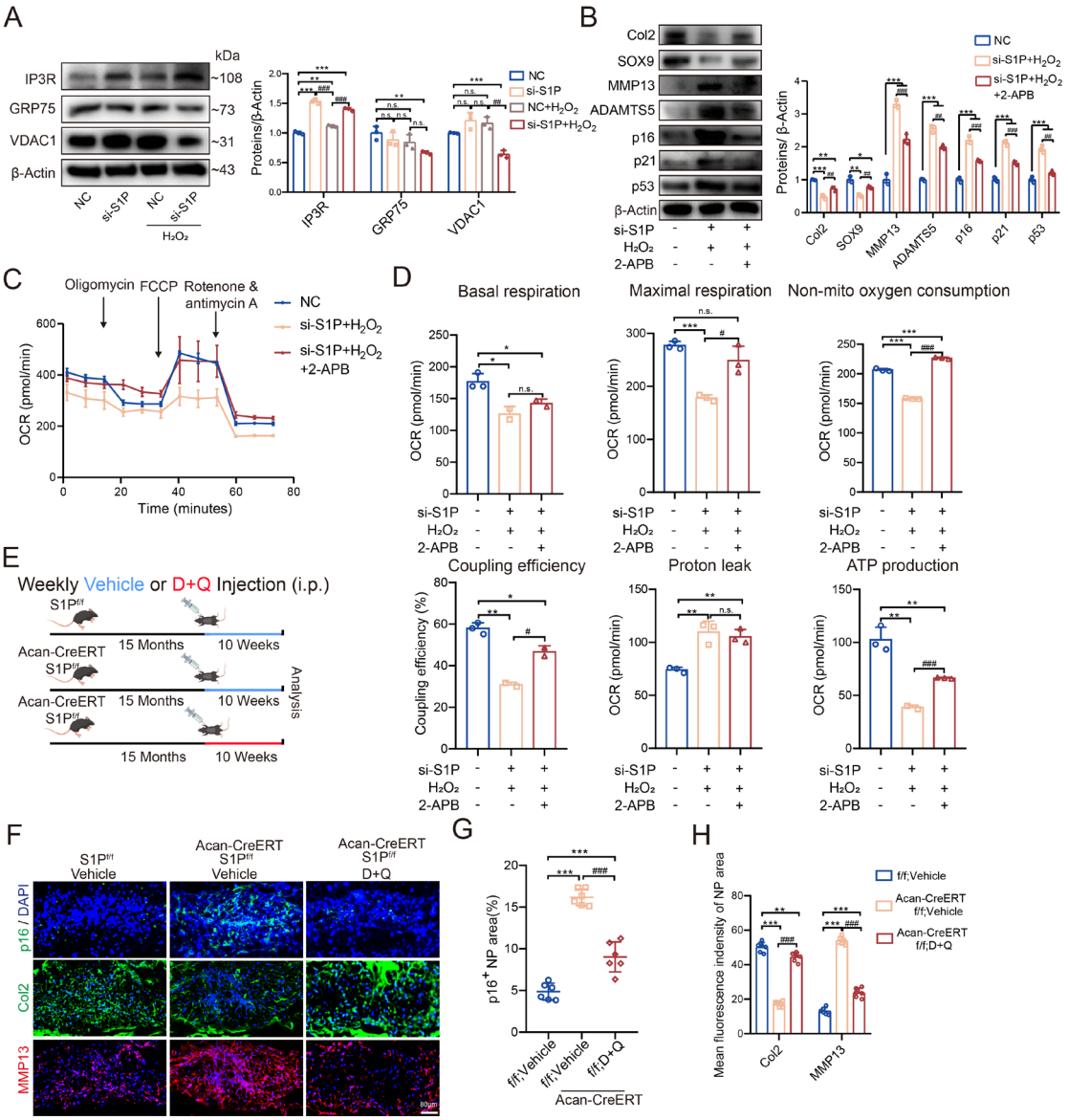

Figure 8

Calcium channel blockers and senolytic drugs can rescue the IVD aging caused by S1P deficiency.

(A) Immunoblots depicting the gene expression of calcium channel proteins IP3R, VDAC1, and GRP75 and the quantification of the blot (n = 3, each group). ** $p < 0.01$, *** $p < 0.001$ compared with NC group. ## $p < 0.01$, ### $p < 0.001$ compared with NC + H_2O_2 group, n.s = no significant. **(B)** Immunoblots depicting the gene expression of senescence-related secretory phenotype genes and quantification of the blot of the si-S1P + H_2O_2 group and the 2-APB rescue group (n = 3, each group). * $p < 0.05$, ** $p < 0.01$, *** $p < 0.001$ compared with NC group. ## $p < 0.01$, ### $p < 0.001$ compared with si-S1P + H_2O_2 group, n.s = no significant. **(C)** Measurement oxygen consumption rate (OCR) by seahorse experiment of three groups (n = 3, each group). **(D)** Statistical analysis of Seahorse experiment data. * $p < 0.05$, ** $p < 0.01$, *** $p < 0.001$ compared with NC group. # $p < 0.05$, ### $p < 0.001$ compared with si-S1P + H_2O_2 group, n.s = no significant. **(E)** Schematic illustration of the study design: peritoneal injections were given on a weekly basis to mice at 15 months of age for 10 weeks. The injections included either a vehicle (1:1 PBS / DMSO) or a combination of D + Q (5 mg/kg Dasatinib plus 50 mg/kg Quercetin). **(F)** Immunofluorescence

images of p16, Col2, and MMP13 in the $S1P^{f/f}$ + vehicle and Acan-creERT-$S1P^{f/f}$ + vehicle groups and the D + Q treatment group. **(G)** Percentage of p16+ area of three groups (n = 6, each group). **(H)** Mean fluorescence intensity of Col2 and MMP13 in the three groups (n = 6, each group). ** $p < 0.01$, *** $p < 0.001$ compared with $S1P^{f/f}$ + vehicle group, ### $p < 0.001$ compared with Acan-CreERT $S1P^{f/f}$ + vehicle group. Results are shown as means ± SD. Student's t-test or one/two-way ANOVA, followed by Tukey's post hoc analysis, was employed to assess statistical significance.